Phosphorus burial in sediments of the sulfidic deep Black Sea: Key roles for adsorption by calcium carbonate and apatite authigenesis

Peter Kraal[*], Nikki Dijkstra, Thilo Behrends, Caroline P. Slomp

Department of Earth Sciences – Geochemistry, Faculty of Geosciences, Utrecht University, PO Box 80021, 3508 TA Utrecht, The Netherlands

Abstract

Sedimentary burial of the essential nutrient phosphorus (P) under anoxic and sulfidic conditions is incompletely understood. Here, we use chemical and micro-scale spectroscopic methods to characterize sedimentary P burial along a water column redox transect (six stations, 78–2107 m water depth) in the Black Sea from the shelf with its oxygenated waters to the anoxic and sulfidic deep basin. Organic P is an important P pool under all redox regimes, accounting for up to 60% of P burial. We find a general down-core increase in the relative importance of organic P, especially on the shelf where P bound to iron (Fe) and manganese (Mn) (oxyhydr)oxides is abundant in the uppermost sediment but rapidly declines in concentration with sediment depth. Our chemical and spectroscopic data indicate that the carbonate-rich sediments (Unit I, $\sim$3000 years, $\sim$0–30 cm depth) of the sulfidic deep Black Sea contain three major P pools: calcium phosphate (apatite), organic P and P that is strongly associated with $CaCO_3$ and possibly clay surfaces. Apatite concentrations increase from 5% to 25% of total P in the uppermost centimeters of the deep basin sediments, highlighting the importance of apatite formation for long-term P burial. Iron(II)-associated P (ludlamite) was detected with X-ray absorption spectroscopy but was shown to be a minor P pool ($\sim$5%), indicating that lateral Fe–P transport from the shelf ("shuttling") likely occurs but does not impact the P burial budget of the deep Black Sea. The $CaCO_3$–P pool was relatively constant throughout the Unit I sediment interval and accounted for up to 55% of total P. Our results highlight that carbonate-bound P can be an important sink for P in $CaCO_3$-rich sediments of anoxic, sulfidic basins and should also be considered as a potential P sink (and P source in case of $CaCO_3$ dissolution) when reconstructing past ocean P dynamics from geological records.
© 2017 Elsevier Ltd. All rights reserved.

Keywords: X-ray spectroscopy; Iron-associated P; Organic P; Redox transect

1. INTRODUCTION

Phosphorus (P), an essential macronutrient that helps control marine primary productivity, is removed from marine systems by burial in the sediment. The mechanisms by which P is sequestered in sediments are strongly dependent on bottom water redox conditions. Understanding the impact of changes in bottom water oxygenation on benthic P cycling is of great importance in light of the globally increasing areal extent of oxygen-depleted coastal marine systems and the importance of P availability in eutrophication (Diaz and Rosenberg, 2008; Middelburg and Levin, 2009). In addition, an accurate interpretation of variations in P burial in paleorecords and the relation with depositional conditions benefits from an accurate understanding of redox-dependent P burial in modern sediments (Algeo and Ingall, 2007; Kraal et al., 2010).

---

* Corresponding author.
  E-mail address: p.kraal@uu.nl (P. Kraal).

Under oxic bottom waters, dissolved phosphate (denoted as HPO_4^{2-}, the dominant phosphate ion at seawater pH) released during organic matter (OM) breakdown is initially scavenged by ferric iron (oxyhydr)oxides (Fe_{OX}) in surface sediments (Einsele, 1936; Mortimer, 1941; Slomp et al., 1996b). This Fe-bound P is released back to the pore-water during sediment burial as Fe_{OX} undergo reductive dissolution. Eventually, the released HPO_4^{2-} precipitates as authigenic P minerals at depth in the sediment or diffuses back to the sediment surface where it typically is either adsorbed to Fe_{OX} or escapes to the overlying water. Under marine conditions with millimolar levels of calcium, the accumulation of dissolved HPO_4^{2-} often leads to calcium phosphate precipitation, predominantly in the form of carbonate fluorapatite (CFA) (Van Cappellen and Berner, 1988; Ruttenberg and Berner, 1993). Calcium phosphates are the stable end product of P diagenesis and constitute the principal long-term P burial phase (Anderson et al., 2001).

In addition, Fe phosphate authigenesis may play an important role in sedimentary P sequestration. In the absence of free dissolved sulfide (referred to here as HS^-, the dominant form at seawater pH), reductive dissolution of Fe_{OX} can lead to the accumulation of both dissolved Fe^{2+} and HPO_4^{2-} and subsequent precipitation of Fe(II)–P phases such as vivianite, $Fe(II)_3(PO_4)_2 \cdot 8H_2O$. Evidence from modern and ancient marine systems suggests that iron(II) phosphate authigenesis is favored under anoxic sulfide-depleted conditions in the water column and sediment (März et al., 2008a,b; Slomp et al., 2013; Hsu et al., 2014; Egger et al., 2015); in the presence of dissolved HS^-, dissolved Fe^{2+} is precipitated in Fe sulfides that have little affinity for HPO_4^{2-} (Krom and Berner, 1980). As such, the balance between Fe^{2+} and HS^- release into pore-waters controls the fate of dissolved HPO_4^{2-} in sedimentary systems.

External input of metal (Fe, Mn) oxides has the potential to alter the relationship between bulk sediment geochemistry and P burial mechanisms. For instance, sulfidic deep basins within the Baltic Sea receive substantial amounts of Fe and Mn (oxyhydr)oxides. The deposition of Fe_{OX} from adjacent, oxygenated shelf sediments and their subsequent reductive dissolution can create Fe^{2+}-rich micro-environments where Fe(II)–P authigenesis occurs within bulk sulfidic sediment (Jilbert and Slomp, 2013; Reed et al., 2015; Dijkstra et al., 2016). Similarly, mixed Mn(II)–Ca–carbonate–phosphate phases may form as a result of anoxic diagenesis of sediment intervals rich in Mn oxides that were deposited in Baltic Sea deep basins following inflows of oxygenated waters (Suess, 1979; Jilbert and Slomp, 2013; Dijkstra et al., 2016). These conditions, in particular the highly dynamic oxygen regime, are rather specific and therefore these findings may not be representative for more open marine, anoxic settings in the past and present.

The Black Sea is well-suited to investigate the effects of long-term euxinia on sedimentary P dynamics including the role of Fe–P associations. It is the world's largest strongly stratified marine basin and its deep (bottom) waters have been sulfidic for thousands of years (Wilkin et al., 1997). Surface sediments in the deep Black Sea consist of an upper layer of laminated coccolith ooze (Unit I, 2.7 ka–present), underlain by a less $CaCO_3$-rich, dark-colored sapropel (Unit II, 7.6 ka–2.7 ka) (Degens and Ross, 1974; Hay et al., 1991; Arthur and Dean, 1998; Eckert et al., 2013). While the sediments of the Black Sea have been studied extensively for decades, there is surprisingly little information on sedimentary P burial. In the two only studies presenting detailed sediment P speciation so far, Dijkstra et al. (2014) and Ruttenberg (1990) reported significant amounts of P apparently present as Fe-associated P (up to 25% of total P) in sediments of the deep basin below more than 2000 m of sulfidic waters. Dijkstra et al. (2014) proposed that this P might be in the form of intra-cellular Fe(II)–P minerals formed within bacteria which were thus shielded from the sulfidic pore waters in which Fe(II)–P is thermodynamically unstable. In contrast to the sediment, Fe–P cycling in the water column of the Black Sea is relatively well-understood. Mixed Fe–Mn (oxyhydr)oxide phases that adsorb HPO_4^{2-} form above and within the redoxcline around 100 m water depth (Shaffer, 1986; Dellwig et al., 2010). The potential for this shuttle to deliver Fe–Mn–P minerals to deep sediments is unclear, but is assumed to be negligible due to reductive dissolution of the oxide phases in the sulfidic waters below the redoxcline (Dellwig et al., 2010). Overall, it is unclear what role Fe(II)–P minerals play in P burial under long-term sulfidic conditions.

In addition, the impact of anoxia on CFA formation is still incompletely understood (Tsandev et al., 2012; Lomnitz et al., 2015). While a limited organic matter flux can explain the lack of authigenic Ca–P formation in some anoxic deep sea settings, such as the Mediterranean Sea during sapropel formation (Kraal et al., 2010; Reed et al., 2011), other factors, such as a high alkalinity have been invoked to explain the lack of Ca–P formation in more productive regions (Schenau et al., 2000). Organic-rich sediments with very little CFA formation have been observed in for instance sulfidic deep basins in the Baltic Sea (Mort et al., 2010) and strongly reducing estuarine sediments (Kraal et al., 2015b). On the other hand, anoxic sediments from oxygen minimum zones host extensive apatite (and phosphorite) formation (Froelich et al., 1988; Schenau et al., 2000; Schulz and Schulz, 2005; Kraal et al., 2012).

Here, we investigate the cycling and burial of P in Black Sea sediments along a depth transect from the shelf with oxygenated bottom waters (78 m water depth, 150 μmol O_2 kg^{-1}) to the anoxic and sulfidic deep basin (2107 m water depth). Detailed chemical characterization of the pore-water and of solid-phase Fe, P and S pools was combined with micron-scale X-ray fluorescence element mapping (μXRF) and X-ray absorption spectroscopy (XAS) for Fe and P speciation. We show that besides authigenic apatite and organic P, P adsorbed onto $CaCO_3$ can represent a key P burial phase in sediments of anoxic and sulfidic basins.

2. MATERIALS AND METHODS

2.1. Sample collection and core processing

During a research cruise with RV Pelagia between June 7 and 23 in 2013, the water column and surface sediment were sampled at six stations along a depth transect in the northwestern Black Sea. The transect extended from the deep sea (2107 mbss) to the shelf (78 mbss) (Fig. 1). Physical properties of the water column were measured with a temperature–conductivity–density (CTD) profiler, to which a Seabird SBE43 oxygen optode was attached for dissolved O_2 measurements.

Multi-cores at all stations were collected using polycarbonate tubes of 60 cm length with an inner diameter of 10 cm. Between 26 and 46 cm of sediment was recovered with overlying water. General sediment properties and a generalized core description based on visual inspection are presented in Table 1. After ensuring that the sediment surface was intact, cores were immediately capped with rubber stoppers and vertically transferred into a N_2-purged oxygen-free glovebox. A 20-mL sample of the overlying water was taken, the remaining overlying water was

siphoned off, and the sediment core was sectioned into intervals between 0.5 and 4 cm thickness, with the resolution decreasing with depth. About 15 mL of wet sediment from each interval was transferred into a pre-weighed glass vial that was stored in an anoxic jar at $-20\ ^{\circ}C$ prior to the on-shore water content determination and solid-phase analyses as described below. The remaining material was transferred into 50 mL polypropylene centrifuge tubes. The closed centrifuge tubes were centrifuged at 4500 rpm for 20 min, and immediately transferred back into the oxygen-free glovebox where the supernatant was filtered over a 0.45 μm Teflon filter. The bulk pore-water was used for various on-board and on-shore analyses, as described below.

2.2. Chemical pore-water and solid-phase analyses

In the oxygen-free chamber, various aliquots of pore-water were taken from the bulk pore-water sample for analyses (Table 2). Dissolved phosphate, ammonium, nitrite, nitrate, total sulfide ($HS^- + H_2S$, denoted here as HS^-) and inorganic carbon were quantified on-board with a QuAAtro autoanalyzer (Seal Analytical). The pore-water
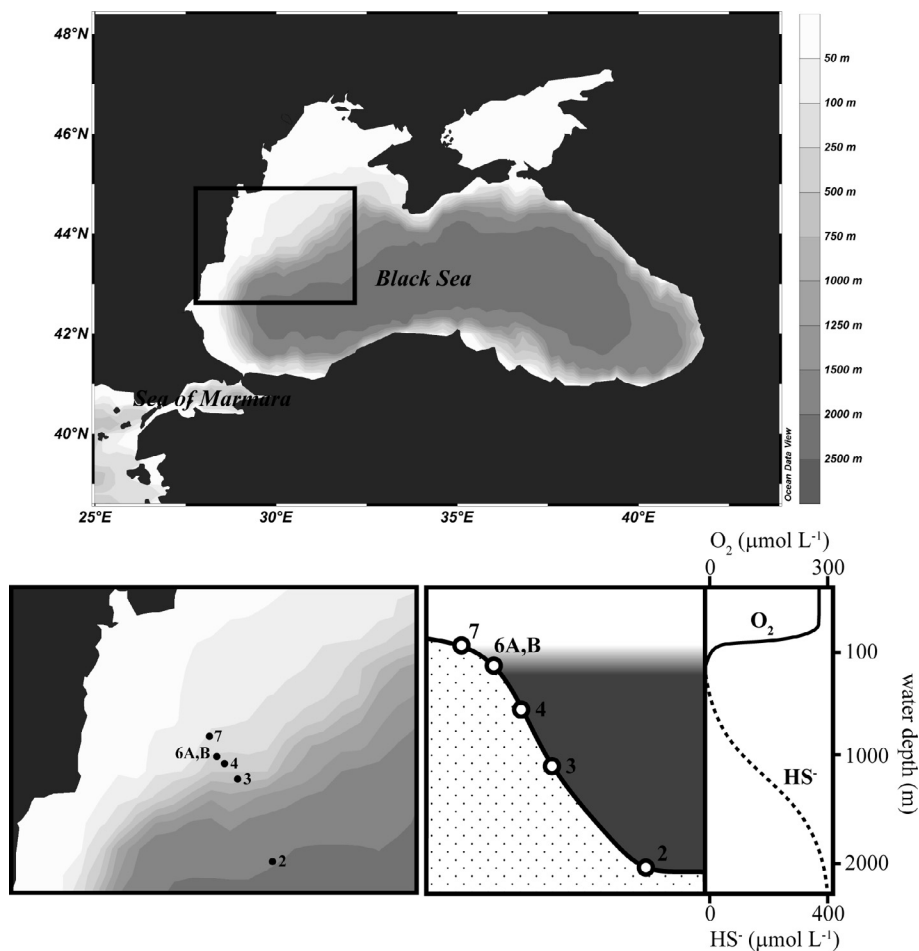

Fig. 1. Map of Black Sea area with sampling stations 2–7 along the transect from the deep sea to the shelf. Black square in top panel is shown as zoom in bottom left panel with station locations. Bottom right panel shows approximate bathymetry and dissolved oxygen and sulfide profiles. Top and bottom left panels were adapted from Ocean Data View 4 (Schlitzer, 2015).

Table 1
General properties of coring locations and retrieved cores (BW = bottom water). The original station numbers were kept for easy comparison with upcoming studies from the same research expedition. Temperature from CTD profiler, oxygen and sulfide from deepest Niskin bottle of CTD/Rosette sampler (depth between parentheses). Station 6A and 6B data from same CTD cast.

Station	Coordinates (lat., long.)	Depth (mbss)	BW T (°C)	BW O$_2$ (µmol kg^{-1})	BW HS$^-$ (µmol L^{-1})	Core length (cm)	Sediment description
7	43°53.8′ N 28°58.6′ E	78	7.8	166.3 (75 mbss)	0	26	Gray clay with shell banks
6A	43°44.1′ N 30°04.4′ E	120	8.5	10.7 (125 mbss)[a]	0	26	Gray clay with shell banks, brown surface layer
6B	43°42.8′ N 30°05.1′ E	130	8.5	10.7 (125 mbss)	0	9.5	Gray clay with shell banks
4	43°40.6′ N 30°07.5′ E	377	8.8	b.d.[b] (300 mbss)	82	46	Laminated mud with fluffy top layer
3	43°31.8′ N 30°15.5′ E	1100	9.0	b.d.[b] (1000 mbss)	381	40	Laminated mud with fluffy top layer
2	42°4.8′ N 29°40.7′ E	2107	9.1	b.d.[b] (2000 mbss)	418	36	Laminated mud with fluffy top layer

[a] CTD depth deeper than station depth; coring location was shifted slightly after CTD to capture the Mn particle maximum.
[b] Below the detection limit of O$_2$ optode of ~0.5 ± 5 µmol kg^{-1}.

N/P ratio was calculated as the ratio between $NH_4^+ + NO_3^- + NO_2^-$ and HPO_4^{2-}. To avoid H_2S loss, the aliquot for sulfide analysis was transferred into a 8 mmol L^{-1} NaOH solution immediately after filtration. Dissolved sulfate concentrations were measured by ion chromatography (Dionex ICS-3000) on-shore at Utrecht University.

Also on-shore, the frozen wet sediment samples in the glass vials were weighed, freeze-dried and immediately transferred to an oxygen-free glovebox. The vials were then closed and transferred out of the glovebox to be weighed to determine water content from weight loss. Subsequently, the vials were transferred back into the glovebox to be manually ground with an agate mortar and pestle. A 0.3 g sub sample of the ground sediment was decalcified by two washes with 1 M HCl (4 h and 12 h) followed by two rinses with ultrapure water. The sediment residue was freeze-dried and organic carbon (C_{org}) content was quantified with a CNS analyzer (Fisons Instruments NA 1500). A second sub sample of 0.125 g was used for total solid-phase analysis after acid digestion. The sub sample was digested in 5 mL of a mixture of concentrated HNO_3, $HClO_4$ and HF at 90 °C. After evaporation of these acids at 160 °C, the residue was dissolved overnight at 90 °C in 1 M HNO_3, and Al, Ca, Fe, Mn, P and S were determined by ICP-OES (Perkin Elmer Optima 3000) in the final solution. Calcium carbonate was calculated on weight basis from total Ca contents after correction for clay-associated Al: $CaCO_3 = 2.5 \times (Ca - 0.345 \times Al)$ (Turekian and Wedepohl, 1961; Reichart et al., 1997).

Two separate sub samples of the ground sediment of 50 and 100 mg were used for sequential extraction of Fe (Poulton and Canfield, 2005; Claff et al., 2010) and P (Ruttenberg, 1992). The extraction steps are detailed in Table 3 and 4. The Fe and P extractions were performed under oxygen-free conditions to prevent artifacts due to sample oxidation (Kraal et al., 2009; Kraal and Slomp, 2014). In addition to the sediment samples, we also subjected synthetic vivianite and $CaCO_3$-bound P to sequential P extraction (for details on synthesis, see Appendix A). The P concentrations in all extracts except the buffered citrate-dithionite extracts were measured with the molybdenum blue colorimetric method (Murphy and Riley, 1958). The citrate-dithionite extracts were analyzed for Ca, Fe, Mn and P by ICP-OES. Reactive P was calculated as total P minus detrital P. The ratio between organic C and reactive P ($C_{org}/P_{reactive}$) was calculated as an indicator of sedimentary P burial efficiency. Assuming reactive P is delivered mostly in organic matter, $C_{org}/P_{reactive}$ values above the Redfield ratio of 106 suggest loss of P from the sediment relative to organic carbon (Ingall and Jahnke, 1994; Kraal et al., 2010).

The total Fe concentrations in all extracts except the CDB solutions were determined with the colorimetric phenanthroline method (APHA, 2005). In the HCl extracts from step 1 of the Fe extraction procedure, Fe^{2+} and total Fe were determined by measuring absorbance before and after adding the hydroxylamine-hydrochloride reducing agent that converts any dissolved Fe^{3+} to Fe^{2+}. The Fe^{3+} concentration was then calculated as the difference between total Fe and Fe^{2+}. The CDB solutions were analyzed by ICP-OES.

Table 2
Pore-water sample treatment and analysis.

Analyte (sample volume)	Pre-treatment	Storage (°C)	Measurement
HPO_4^{2-}	Acidified to pH ~ 1 with 5 M suprapur HCl	4	Autoanalyzer (on-board)
NH_4^+, NO_2^-, NO_3^-	None	4	Autoanalyzer (on-board)
HS^-	Diluted 4× in degassed 8 mmol L^{-1} NaOH	4	Autoanalyzer (on-board)
DIC	Diluted 10× in degassed 25 g L^{-1} NaCl	4	Autoanalyzer (on-board)
SO_4^{2-}	Diluted 10× in ultrapure water	4	Ion chromatography (Utrecht Univ.)

The sum of the extracted Fe phases is termed highly reactive Fe (Fe_{HR}): iron that has already reacted with sulfide and Fe phases that are reactive towards dissolved sulfide on geologically short timescales (years to millennia) (Canfield et al., 1992; Raiswell and Canfield, 1998; Poulton and Canfield, 2005). Because of uncertainty regarding the partial dissolution of magnetite in the HCl and CDB solutions (step 1 and 2 of sequential Fe extraction), the CDB-Fe and oxalate-Fe are collectively referred to as crystalline Fe(III) (oxyhydr)oxides. The difference between total Fe as measured by acid digestion and Fe_{HR} represents poorly reactive and unreactive Fe (here jointly termed Fe_{PR}). The degree of pyritization (DOP) was calculated here as the fraction of highly reactive Fe that was present as HNO_3-Fe: $DOP = pyrite$-Fe/Fe_{HR}, a slight alteration of the original formulation of $DOP = pyrite$-$Fe/(pyrite$-$Fe + acid$-$soluble\ Fe)$ (Berner, 1970; Raiswell et al., 1988).

On a subset of samples from all stations, reduced inorganic sulfur (RIS) pools were determined using a slight modification of the sequential extraction method of Burton et al. (2011), as described by Kraal et al. (2013). The method separates RIS into acid-volatile sulfide (AVS; 6 M HCl, 24 h), elemental sulfur (S^0; reagent-grade methanol, 16 h) and chromium-reducible sulfide (CRS or pyrite-S; chromous chloride in 32% HCl, 48 h). Acid-volatile sulfide gives an estimate of Fe monosulfide, FeS (Rickard and

Morse, 2005). The sulfide released as H_2S during AVS and CRS extraction was trapped as ZnS in alkaline Zn acetate traps. Sulfide content of the traps was determined by iodometric titration. Elemental sulfur was quantified by the cyanide-ferric chloride colorimetric method (Bartlett and Skoog, 1954).

Sediment weights used in the calculation of all solid-phase concentrations were corrected for salt content: the weight of salt as calculated from gravimetric water content and salinity was subtracted from the dry weight of freeze-dried sediment.

2.3. Micro-scale element mapping and X-ray absorption spectroscopy

A multi-core from station 2 (2169 mbss) was used for resin embedding under anoxic conditions following the method by Jilbert and Slomp (2013). The embedding procedure and preliminary sample preparation for synchrotron-based micro-scale analyses are described in Appendix A.

The top part of the resin-embedded core top (0–1 cm, 1 cm diameter) was transported in a gas-tight, N_2-filled Al laminate bag (Gruber Folien GmbH, Straubing, Germany) to beamline ID21 (X-ray microscopy) of the European Synchrotron Radiation Facility (ESRF) in Grenoble, France. The design of the beamline is described by Salomé et al. (2013). Micro-scale element maps were collected from areas

Table 3
Chemicals and target phases of the sequential Fe extraction procedure, a combination of extraction steps presented in Poulton and Canfield (2005) and Claff et al. (2010).

Extractant (extraction time)	Target phase	Term	Reference
1 mol L^{-1} HCl, pH 0 (4 h)	Poorly ordered or pH-sensitive Fe(II) and Fe(III) minerals, such as ferrihydrite, Fe carbonate and Fe monosulfide	HCl-Fe(II) and HCl-Fe(III)	Claff et al. (2010)
0.35 mol L^{-1} acetic acid/0.2 mol L^{-1} Na_3-citrate/50 g L^{-1} Na dithionite, pH 4.8 (4 h)	Crystalline oxide minerals (goethite, hematite)	CDB-Fe; crystalline Fe (III)[b]	Poulton and Canfield (2005), Claff et al. (2010)
0.17 mol L^{-1} NH_4 oxalate/0.2 mol L^{-1} oxalic acid, pH 3.2 (6 h)	Recalcitrant oxide minerals (magnetite)[a]	oxalate-Fe[a]; crystalline Fe (III)[b]	Poulton and Canfield (2005)
65% HNO_3 (2 h)	Pyrite	HNO_3-Fe	Claff et al. (2010)

[a] Due to likely partial dissolution of magnetite in 1 M HCl (Poulton and Canfield, 2005) and the acetic acid–citrate–dithionite solution (Claff et al., 2010), this likely only represents the most recalcitrant magnetite.
[b] In light of the above uncertainty, CDB-Fe and oxalate-Fe are collectively referred to as crystalline Fe(III).

Table 4

Chemicals and target phases of the sequential P extraction procedure, a streamlined version of the SEDEX procedure of Ruttenberg (1992), i.e. with all H_2O wash steps and selected $MgCl_2$ steps removed (Slomp et al., 1996a).

Extraction (extraction time)	Target phase	Term
1 mol L^{-1} $MgCl_2$ brought to pH 8 (0.5 h)	Exchangeable P	Exchangeable P
0.3 mol L^{-1} Na_3 citrate/1 mol L^{-1} $NaHCO_3$/25 g L^{-1} Na dithionite, pH 7.6 (8 h)[a]	P bound to easily reducible Fe(III) (oxyhydr)oxides, vivianite[b] ($Fe(II)_3(PO_4)_2 \cdot 8H_2O$)	CDB–P[c]
1 mol L^{-1} Na acetate buffered to pH 4 with CH_3COOH (6 h)[a]	Carbonate fluorapatite, hydroxyapatite	Ca–P
1 mol L^{-1} HCl (24 h)	P in detrital minerals	Detrital P
Ashing residue at 550 °C (2 h), followed by 1 mol L^{-1} HCl (24 h)	P in organic matter	Organic P

[a] Followed by 1 mol L^{-1} $MgCl_2$ (adjusted to pH 8 with NaOH) wash step to extract P that was resorbed during extraction.
[b] Potential for vivianite dissolution in this solution shown by Nembrini et al. (1983) and Dijkstra et al. (2014).
[c] Because of the potential of CDB to extract P phases other than Fe–P, the general term CDB–P is used.

of interest and selected Fe and/or P-rich regions were analyzed with spot X-ray absorption spectroscopy across the Fe K edge from 7.00 to 7.65 keV (extended X-ray absorption fine structure, Fe EXAFS) or across the P K edge from 2.13 to 2.40 keV (X-ray absorption near-edge spectroscopy, P XANES) in fluorescence mode. Further details can be found in Appendix A.

3. RESULTS

3.1. General sediment properties

The C_{org} content of surface sediments (0–2 cm sediment depth) from the stations >377 mbss was on average 5–7 wt. %. The stations located closer to and above the redoxcline had a lower C_{org} content of on average 1–2 wt.% (Fig. 2). Aluminum contents were highest at intermediate depths: 3–4 wt.% between 120 and 377 mbss, decreasing to values <2 wt.% at the shallowest and deepest stations. Aluminum contents were consistently lower in surface sediments compared to whole-core averages. Calcium carbonate contents showed a reverse trend with water depth compared to Al contents, with lowest contents at intermediate depths.

Manganese (Mn) was strongly enriched in surface sediments overlain by oxygenated waters (<130 mbss) and in particular at station 6A located within the redoxcline, where contents ranged up to ~750 µmol Mn g^{-1}. The Mn enrichments were restricted to the upper 1 cm of the sediment and declined rapidly with sediment depth. This led to a large standard deviation of the average Mn content for the surface sediment (top 2 cm, $n = 4$) and a marked difference between surface and whole-core averages.

Sedimentary P content showed a slight decrease with increasing water depth. The obvious exception was the sediment from redoxcline station 6A (120 mbss), which was strongly enriched in P. This enrichment was restricted to the surface sediment, as is evident from the lower whole-core average P content. Organic carbon to reactive phosphorus ratios ($C_{org}/P_{reactive}$) were constant at ~75 mol mol^{-1} at water depths <130 mbss and showed a strong increase with water depth up to ~250 mol mol^{-1} at the deepest station.

Average surface sediment Fe content was around 250 µmol g^{-1}, with peaks at 120 and 377 mbss. The sediment at 120 mbss showed a surficial Fe enrichment of 600 µmol g^{-1} and Fe content sharply declined with sediment depth. The high average at 377 mbss was caused by a strong enrichment of >1000 µmol g^{-1} in one sample (0.5–1.0 cm sediment depth), leading to the large standard deviation. The fraction of sediment Fe present as highly reactive Fe (Fe_{HR}/Fe_T, for definition see Materials and methods) showed minimum values down to 0.4 for stations at intermediate water depths. Above and below, the Fe_{HR}/Fe_T ratio increased strongly, reaching values of up to 0.7.

The molar ratio between Fe and S showed a peak in the surface sediments from the redoxcline with values up to 16, and then sharply decreased to values <1 with water depth. The whole-core Fe/S ratios at the shallower stations were low compared to the surface sediment. The degree of pyritization (DOP) of the surface sediment increased with water depth from 0 to 0.8, with a pronounced jump below the redoxcline. Strong down-core increases in DOP were observed for stations within and above the redoxcline, while deeper stations showed more stable, high DOP. This is reflected by large differences between surface sediment and whole-core average DOP values for the shallower stations.

3.2. Pore-water composition

Pore-water SO_4^{2-} concentrations at the sediment surface decreased from the deep basin (17 mmol L^{-1} at SWI) to the shelf (15 mmol L^{-1}), and showed down-core decreases of 1–3 mmol L^{-1} (Fig. 3). Dissolved HS^- concentrations were consistently high in the pore-waters from the deep stations (2 and 3), and showed a strong down-core increase at intermediate station 4 (377 mbss). The shallow stations within and above the redoxcline (6A, 6B, 7) showed low dissolved HS^- concentrations in the upper sediments, with minor HS^- accumulation at depth at station 6A. The trends in pore-water NH_4^+ were similar to those of dissolved HS^-, be it that significant NH_4^+ accumulation occurred at depth in the cores from the shallow stations as well. Dissolved HPO_4^{2-} concentrations showed a down-core increase at all
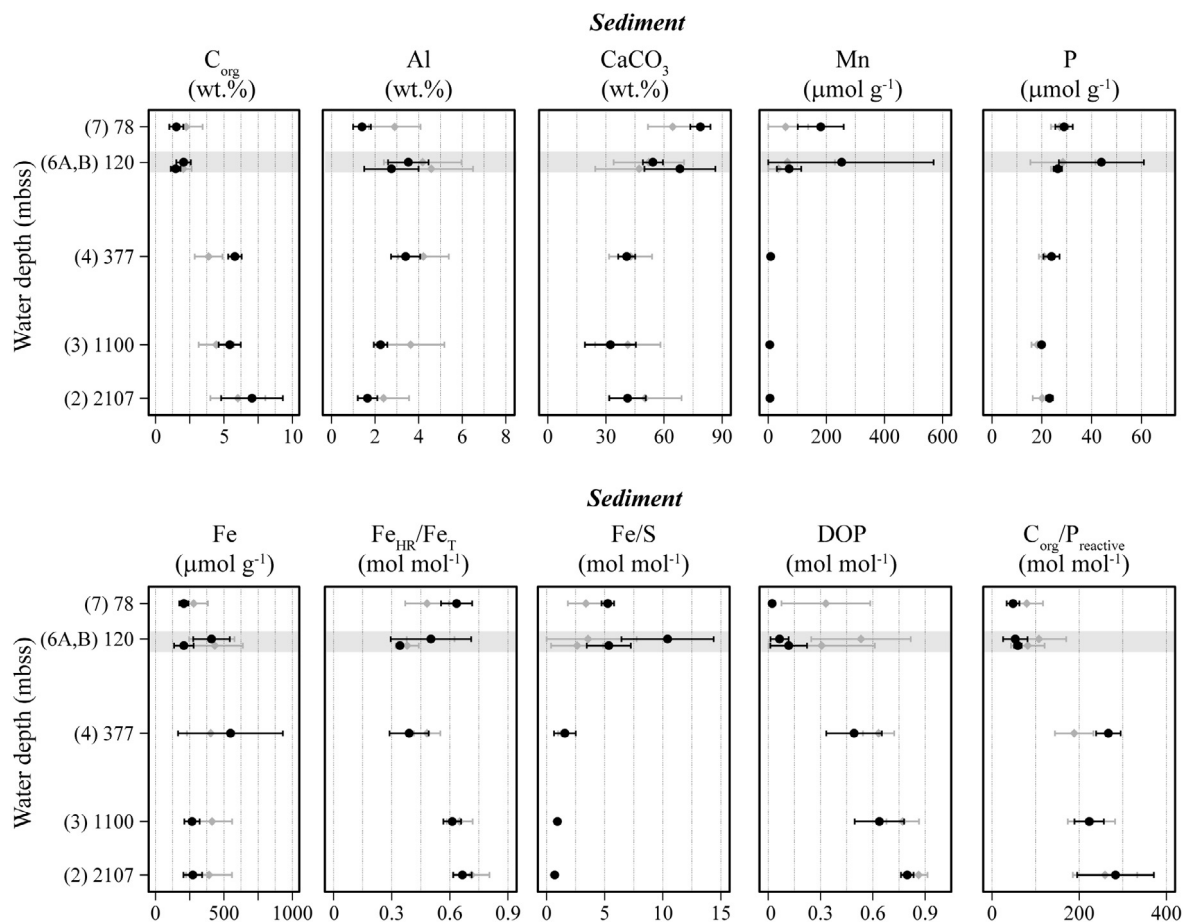
Fig. 2. Key geochemical sediment parameters plotted per station against water depth in meters below sea surface (mbss). Fe_{HR} = highly reactive Fe, Fe_T is total Fe, DOP = degree of pyritization, $C_{org}/P_{reactive}$ is the ratio between organic C and reactive P (total P minus detrital P). All concentrations are expressed on a dry weight basis. Black circles represent averages of surface sediments (0–2 cm depth, $n = 4$), gray circles represent whole-core averages for each station ($n = 12$–24). Gray horizontal bars indicate the approximate position of the redoxcline. Error bars show the standard deviation. Note the logarithmic y-axis, which is only labelled at water depths of stations (station number between parentheses).

stations, with highest gradients in the surface sediments from shallow stations 7 and 6A. Only at station 6B, the HPO_4^{2-} concentration in the bottom water was markedly higher than in the uppermost sediment interval. At sediment depths >10 cm, dissolved HPO_4^{2-} concentrations were similar at all stations. Molar pore-water N/P ratios showed a decrease from the deep basin to the slope and shelf stations. Dissolved Mn^{2+} concentrations were negligible at the stations below the redoxcline, but showed strong subsurface enrichments in the sediments from within and above the redoxcline. Dissolved Fe^{2+} concentrations were below the detection limit ($\sim 2\ \mu mol\ L^{-1}$) at all stations.

3.3. Sedimentary pools of iron, phosphorus and sulfur

There was large variability in the content and chemical forms of Fe in the investigated sediments, both within cores and between stations (Fig. 4). At the stations overlain by oxygenated waters (7, 6A and to a much lesser extent 6B), the surface sediment was enriched in HCl–Fe(III). Below the oxic surface layer at these stations, HCl–Fe(II)

showed a rapid increase at the expense of HCl–Fe(III). Station 7 showed a general increase in total Fe with sediment depth, with a relatively stable fraction of 0.6 ± 0.1 of highly reactive Fe (i.e. the combined pool of HCl-extractable Fe, crystalline Fe_{OX} and pyrite, see also Section 2.3). Station 6A, which was located near the redoxcline, showed a broad mid-core peak in Fe that consisted mostly of HNO_3-Fe and poorly reactive Fe, which rapidly declined below 15 cm sediment depth. At the shelf and redoxcline stations (7, 6A, 6B), around 5–15% of highly reactive Fe was present in the form of crystalline Fe_{OX}, decreasing with sediment depth.

The sedimentary Fe pool at the deeper stations (4, 3, 2) was dominated by HNO_3–Fe and poorly reactive Fe and showed consistent trends that were offset in depth. From slope station 4 to deep basin station 2, Fe profiles were influenced by decreasing sedimentation rates: key peaks and troughs were located at progressively shallower sediment depth and increased in magnitude. The decline in HCl–Fe(II) and crystalline Fe_{OX} with increasing water depth was counterbalanced by a marked increase in the

content of HNO_3–Fe. As a result, total Fe contents remained similar with increasing water depth (whole core averages 340–370 $\mu mol\ g^{-1}$), and the percentage of HNO_3-Fe increased from 30% to 60% of total Fe. Concurrently, a sharp decrease in poorly reactive Fe with water depth was observed.

The total solid-phase phosphorus contents were similar at all stations, with relatively high down-core variability at the shallower stations 7 and 6A (Fig. 5). Organic P was a relatively important P pool (20–60% of total P) at the shallowest shelf station (7, 78 mbss). In the upper sediment interval at this station, CDB–P was enriched and made up as much as 65% of total P, a percentage that declined with sediment depth to 15% of total P. Acetate–P (10–20% of total P) and HCl–P (5–15% of total P) showed a gradual down-core increase.

At station 6A (120 mbss) the upper-most sediment was also strongly enriched in CDB–P, reaching 40 $\mu mol\ g^{-1}$ (75% of total P). There was a gradual down-core decrease in all P species with a clear drop in HCl–P and organic P below ∼15 cm. Station 6B showed a much smaller surface enrichment in CDB–P compared to station 6A, but the P profiles were similar to the corresponding depth interval at station 6A in all other aspects.

The sedimentary P contents at the other slope and deep stations (4, 3 and 2) were relatively constant with depth. CDB–P was an important P phase throughout the Unit I sediment interval. It accounted for 20–40% of total P and showed a strong covariation with Ca contents. Below the Unit I/II transition, CDB–P rapidly declined but peaked again at the relatively carbonate-rich Unit I/II boundary. At all three slope and deep stations, acetate–P showed an overall down-core increase, with the sharpest increase in the top ∼5 cm and pronounced peaks around the Unit I/II transition. Acetate–P accounted for up to 30% of total P. The HCl–P content was relatively stable down-core at the three deepest stations, with an average decrease with water depth from 16% (station 4) to 7% (station 2) of total P. Organic P contents were similar at these stations, both in absolute and relative terms. Similar to the Fe data, the P records also showed the effects of concentration due to decreased sedimentation rate: maxima in the records of CDB–P, acetate–P and organic P occurred progressively shallower and became more pronounced.

The reduced inorganic S (RIS) pool at all stations consisted predominantly of chromium-reducible S (pyrite-S) that accounted for >95% of RIS, with minor contributions of AVS and S^0 (data not shown).

3.4. Sequential extraction of reference materials

The citrate-bicarbonate-dithionite solution (pH 7.6) dissolved 95% of P in fresh synthetic vivianite and 80% of P in the geological vivianite sample. Chemical equilibrium modeling with Mineql showed that the solubility of vivianite in CDB is equivalent to a solid-phase concentration of >300 $\mu mol\ g^{-1}$, sufficient for complete dissolution of naturally occurring amounts of sedimentary vivianite that are usually <100 $\mu mol\ g^{-1}$.

During phosphate adsorption onto $CaCO_3$ (see Appendix A), the dissolved PO_4^{3-} concentration in the 5 g L^{-1} $CaCO_3$ suspension dropped from 100 $\mu mol\ L^{-1}$ to 35 $\mu mol\ L^{-1}$, equivalent to formation of ∼13 $\mu mol\ g^{-1}$ $CaCO_3$-adsorbed P. The SEDEX procedure extracted approximately 5 $\mu mol\ g^{-1}$ exchangeable P, 6 $\mu mol\ g^{-1}$ CDB–P and 0.5 $\mu mol\ g^{-1}$ acetate–P; total extracted P was
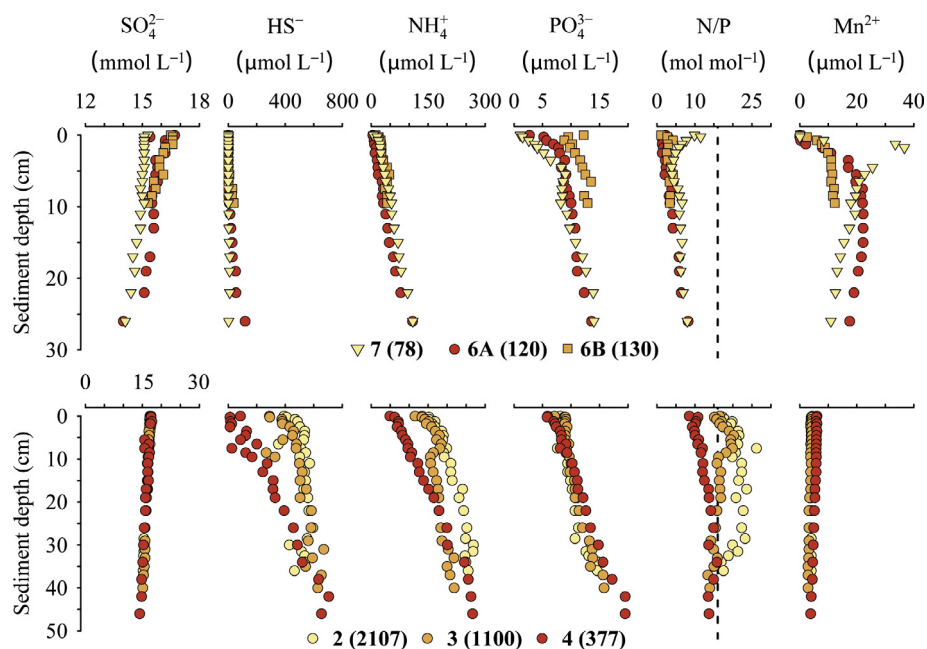

Fig. 3. Concentrations of key pore-water components plotted against sediment depth for all stations: shallow station 7, 6A and 6B in upper panels, deep stations 2, 3 and 4 in lower panels. Uppermost sample (depth = 0) is bottom water. The vertical dashed line in the panel (e) indicates the Redfield N/P ratio for marine organic matter (16/1). Note the different x axes for sulfate concentration at the shallow and deep stations.
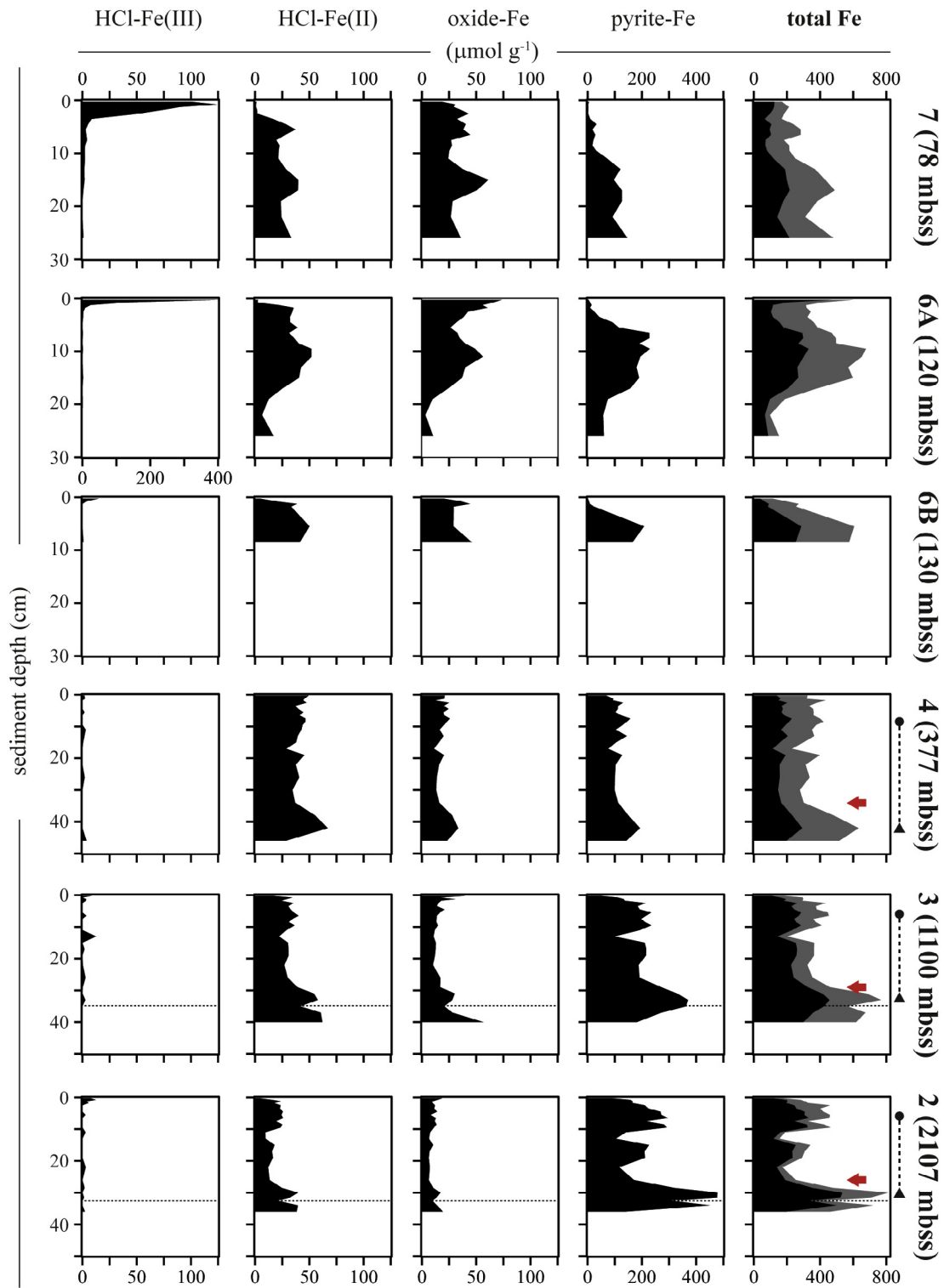
Fig. 4. Sedimentary iron fractions against sediment depth at all investigated stations, rightmost panels with reactive Fe (sum of sequentially extracted Fe fractions) in dark grey and poorly reactive Fe (difference between total Fe and total reactive Fe) in black. For details on Fe fractions, see Materials and methods and Table 3. Note the different x axes for HCl-Fe(III) at station 6A. In panels with profiles from stations 4, 3 and 2, the horizontal dashed line indicates the Unit I/Unit II transition, and the red arrow indicates the uppermost occurrence of sapropelic (carbonate-poor) sediment. The circle and triangle symbols, connected with dashed lines, to the right of the total Fe profiles indicate the depth of common features in the total Fe profile used for estimation of differences in sedimentation rates.
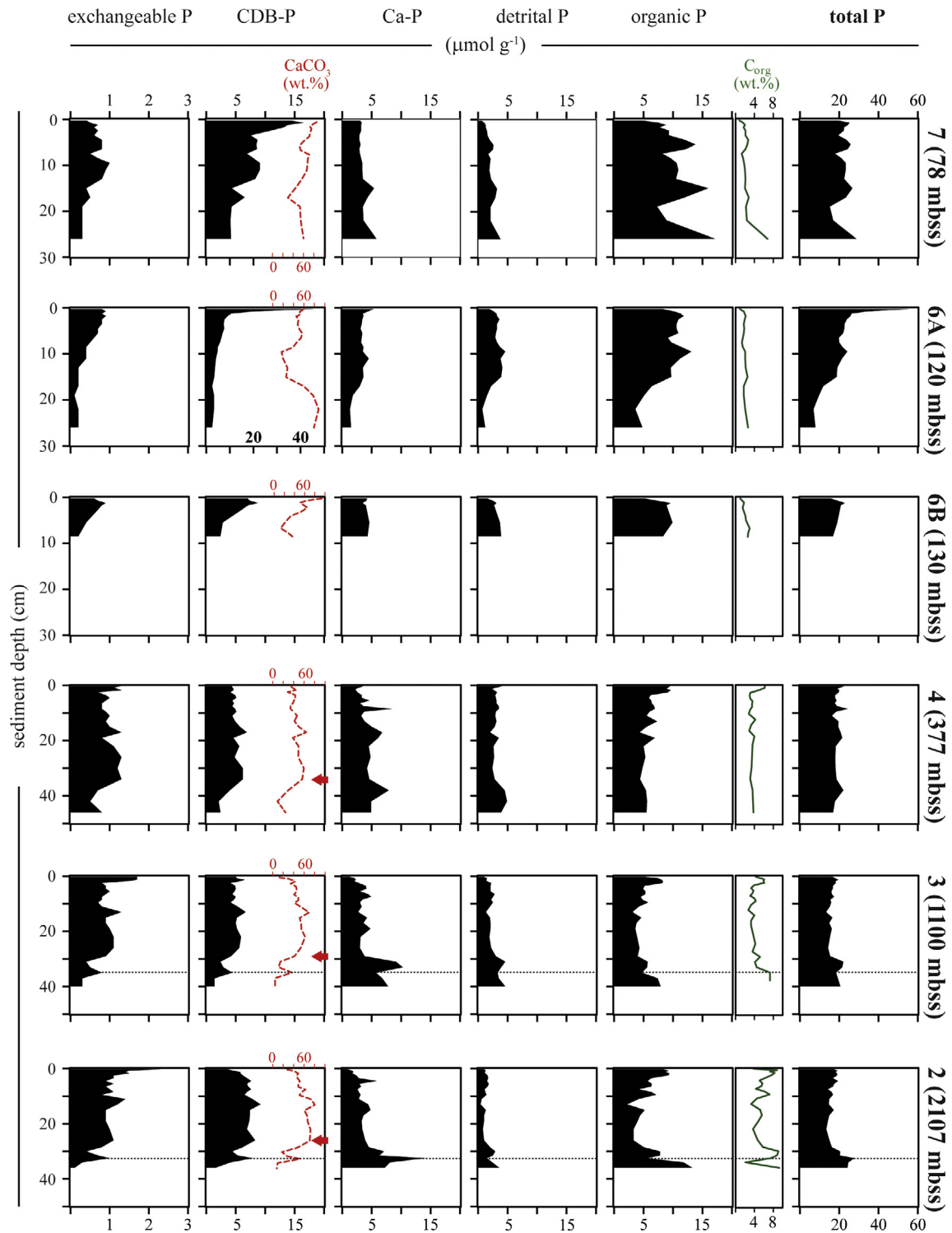
Fig. 5. Sedimentary phosphorus fractions against sediment depth at all investigated stations. Total P is sum of sequentially extracted P fractions (within 10% of total P from acid digest). Because of the potential of CDB to extract P phases other than Fe–P, the general term CDB–P is used. Next to organic P, organic C has been included. For details on Fe, P and S fractions, see Materials and methods. Note the different x axes for CDB–P at stations 7 and 6A. Dashed red profiles in the CDB–P panels show the CaCO₃ content in wt.%. In panels with profiles from stations 4, 3 and 2, the horizontal dashed line indicates the Unit I / Unit II transition, and the red arrow indicates the uppermost occurrence of sapropelic (carbonate-poor) sediment.
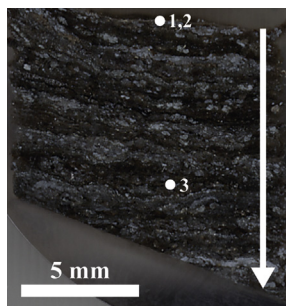
Fig. 6. Visible light color scan (CanoScan Lide 210) of resin-embedded core top (0–1 cm). Light and dark colored laminae are calcite-rich and -poor intervals, respectively. Solid white circles indicate areas mapped and analyzed with synchrotron-based X-ray fluorescence techniques. White arrow indicates downward vertical dimension from sediment–water interface to ~1 cm sediment depth. Analysis at Fe K edge: map 1, analysis at P K edge: maps 2 and 3. Map 1 and 2 were collected during separate scans (sample changes in between) and therefore cover similar but not identical sample areas.

~11 µmol g^{-1} of which about half was extracted as CDB–P. Calculated from the Ca concentration, the CDB solution dissolved <5% of the $CaCO_3$.

3.5. Micro-scale analysis of surface sediment from station 2

Synchrotron-based µXRF maps (0.4–4 µm^2) were collected from three regions (Fig. 6). Calcium and Fe show distinctly enriched regions (Map 1; Fig. 7). The Fe map at 7500 eV showed abundant micro-scale Fe enrichments, many of which were spatially correlated to S enrichments (Fig. 7). The eigen analysis indicated that three components are required for a satisfactory reproduction of all Fe spectra (Fig. 8). All three components showed close resemblance to standard spectra from our Fe XAS reference library: pyrite (component 1), illite (component 2) and biotite (component 3). The smaller first peak of the white line in component 3 compared to biotite may indicate that component 3 represents clay-bound Fe with a smaller Fe(II) over Fe(III) predominance. The analyzed spots represented both pure phases and mixtures of the three ITFA-extracted

components (Table 5). The XANES spectrum of component 2 is also similar to that of Fe$_{OX}$ such as lepidocrocite, but the EXAFS spectrum shows marked difference between component 2 and Fe$_{OX}$, indicating that the ferric iron is structurally (clay-)bound. This is also in line with the chemical Fe results that showed no HCl-Fe(III) and only very little crystalline Fe(III). Overall, the results indicate that Fe in the surface sediment from station 2 is present in pyrite, primary Fe(II)/Fe(III) silicates with a predominance of Fe(II) represented here by biotite, and Fe(III)-containing clays represented here by illite.

The µXRF data collected at 2300 eV from two areas around the sediment surface (Map 2 and 3; see Fig. 6) show a number of P enrichments against a disperse background (Fig. 9). The enrichments consist of apatite, $Ca_5(PO_4)_3(OH,F)$ (square symbols in Fig. 9). A single enrichment in Map 3 yielded an X-ray absorption spectrum that closely resembles the iron phosphate ludlamite (circle symbol in Figs. 9 and 10). Ludlamite is a ferrous iron phosphate with minor amounts (<5 wt.%) of Mg and Mn, described by the generalized formula $(Fe(II),Mg,Mn)_3(PO_4)_2 \cdot 4(H_2O)$.

Spot P XANES measurements from areas with less intense P enrichment ("disperse P"; star symbols in Fig. 9), show a relatively smooth P K-edge XANES spectrum with a white line at 2153 eV and oxygen oscillation around 2170 eV. The spectrum lacks the pre-edge features observed for P associated with Fe(III) and Mn (oxyhydr)oxides (Giguet-Covex et al., 2013; Egger et al., 2015; Rivard et al., 2015), the post-edge shoulder indicative of Ca-associated P (Hesterberg et al., 1999; Ingall et al., 2011), the post-edge peak of polyphosphate (Kraal et al., 2015a) and the pre- and post-edge features associated with Fe(II)–P minerals (Fig. 10). The disperse P spectrum shows similarity to the spectrum of organic P. In Fig. 10 phytic acid is used as an example, other common organic P phases such as adenosine triphosphate have similar spectra (Brandes et al., 2007). Furthermore, spectroscopic analysis of P adsorbed onto Al oxide and clay minerals collected by Giguet-Covex et al. (2013) showed similar featureless spectra as the disperse P in our sample.

In summary, the synchrotron-based P analysis shows Ca phosphate enrichments and a single Fe(II) phosphate
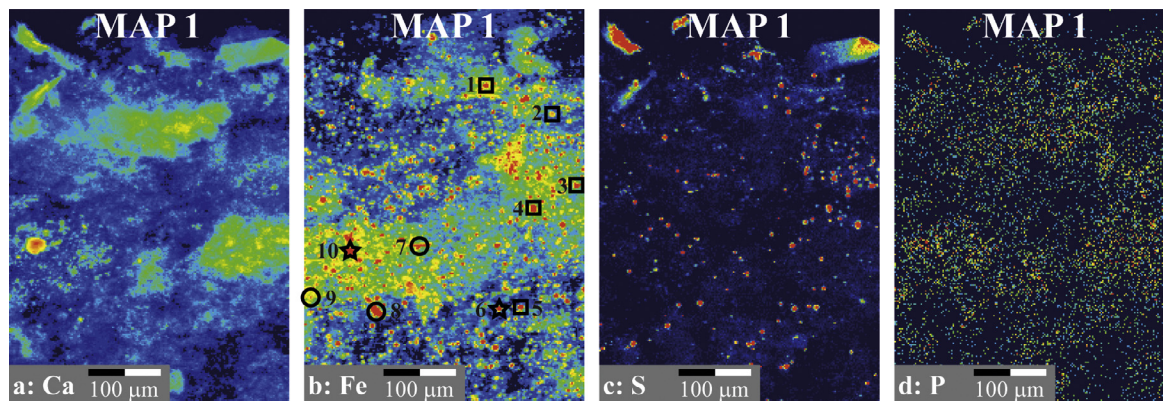

Fig. 7. Synchrotron-based µXRF mapping (2 µm step size) of calcium (a), iron (b), sulfur (c) and phosphorus (d) for Map 1 from the sediment surface (see Fig. 6). Total scanned area is 0.39 × 0.55 mm; scale bar in bottom left corner. Symbols in panel (b) indicate spot XAS measurements of different types of Fe-bearing minerals: pyrite-Fe (square), clay-associated Fe (star) and mixed pyrite/clay phases (circle).

particle, against a background of disperse P that is likely a combination of adsorbed and organic P. The spectra collected from bulk samples from the surface (1.25 cm) and deeper (32.5 cm) sediment at station 2 are very similar to that of adsorbed/organic P, but the development of a post-edge shoulder and a slight shift of the absorption edge indicate an increased contribution by Ca phosphate (apatite) to the total P pool (Fig. 10).

4. DISCUSSION

4.1. A key role for adsorbed P in deep Black Sea sediments

The SEDEX step targeting Fe-associated P, using a citrate–dithionite–bicarbonate solution (CDB: Ruttenberg, 1992), is intended to extract easily reducible Fe(III) (oxyhydr)oxides and the associated P. However, this study and previous work (Nembrini et al., 1983; Dijkstra et al., 2014) show that CDB can also dissolve reduced Fe–P minerals such as vivianite. Ligand-promoted dissolution of calcite (Petersen et al., 1966) and mineral fish debris that consist largely of hydroxyapatite (biogenic apatite: $Ca_5(PO_4)_3OH$) (Schenau and De Lange, 2000) may also occur. The adsorption experiment conducted for this study showed that ∼50% of $CaCO_3$-adsorbed P resisted extraction by $MgCl_2$ and was extracted in the subsequent CDB step. This P is thus strongly adsorbed or incorporated into the calcite surface. The small percentage of concurrently extracted Ca (<5%) suggests that CDB only dissolves the calcite surface and associated P. In summary, CDB–P can encompass a range of P phases from Fe(III)-bound P to Fe(II)–P minerals and $CaCO_3$-associated P.

The surface sediments from the two shallowest stations under oxygenated bottom waters, 7 (78 mbss) and 6A (120 mbss), likely contained true Fe(III)-associated P that was extracted by CDB. Here, strong enrichments in poorly crystalline Fe_{OX} were observed and the Fe/P ratio in the CDB extracts of 6–8 (Fig. 11) is indicative of P bound to poorly ordered Fe_{OX} (Jensen and Thamdrup, 1993; Slomp et al., 1996a). The surficial Mn enrichments at these sites suggest that P adsorption onto Mn oxides may also contribute to the CDB–P pool. Below the surface sediment, the CDB Fe/P ratio quickly falls below known values for Fe(III)-bound P and even Fe(II)–P minerals (vivianite: Fe/P ≈ 1.5), and Fe was often below detection in the CDB extracts. This was also observed for almost all samples from the anoxic and sulfidic deep basin and suggests

Table 5
Weights of different Fe phases (i.e. fractions of total Fe) based on ITFA (see Appendix A for details). Gray fill indicates the major Fe phase(s) identified at each spot.

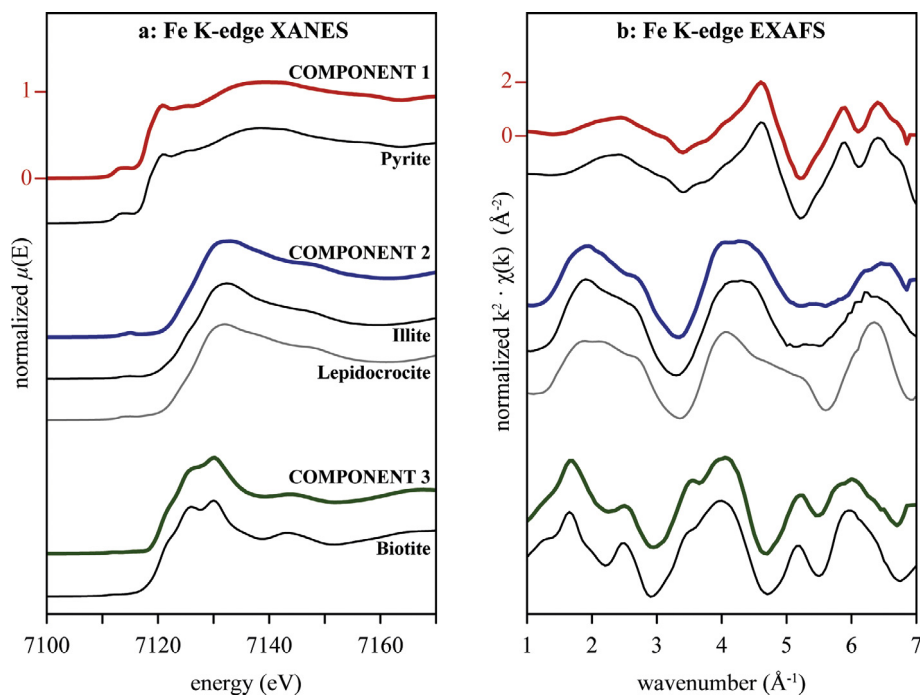| Spot	Comp. 1 (pyrite)	Comp. 2 (illite)	Comp. 3 (biotite)
1	0.95	0.05	0.00
2	0.97	0.07	−0.04
3	1.00	0.00	0.00
4	1.00	0.01	−0.01
5	0.98	0.05	−0.03
6	0.00	1.00	0.00
7	0.00	0.59	0.41
8	0.21	0.00	0.79
9	0.52	0.48	0.00
10	0.07	0.92	0.01

Fig. 8. Spectra of the three components obtained from iterative target transformation factor analysis in comparison to normalized XANES (a) and EXAFS (b) spectra of different reference materials.

extraction of P phases other than Fe-associated P. In the deep basin, nearly all Fe is present in clays or pyrite, with potentially a small pool of crystalline Fe_{OX} that have low affinity for HPO_4^{2-} (Fe/P $\gg$ 10) and cannot account for the measured pool of CDB–P.

Combining our chemical results with micro-scale spectroscopy suggests that CDB-extractable P does not originate from the dissolution of Fe(III) oxides but rather represents P associated with calcite and possibly clay surfaces. The disperse P pool identified by spectroscopy shows P K-edge spectra similar to those of organic P and adsorbed P (Fig. 10). Organic P is only sparingly soluble in CDB and may therefore contribute to the total disperse P pool but not to the CDB–P pool. The CDB solution can extract adsorbed P by ligand-promoted dissolution of calcite and silicate surfaces. The strong correlation (Pearson's $r = 0.68$) between exchangeable and CDB-extractable P at the deep stations (Fig. 4) likely reflects the separation of weakly and strongly adsorbed P, respectively, where the latter exceeds the former by about an order of magnitude. Strongly adsorbed P may (in part) represent surface-incorporated P; the peak height of the disperse P spectrum is low compared to the spectra of P adsorbed onto reference materials (Fig. 10). This suggests suppression of the detectable P K-edge fluorescence signal due to absorption by neighboring atoms caused by incorporation of P into the surface of sediment components.

There are strong indications that $CaCO_3$-associated P is an important contributor to the CDB-extractable, adsorbed P pool in the investigated anoxic and sulfidic sediments. There was a positive correlation (Kendall's $\tau = 0.47$) between Ca and P in the CDB extracts from station 4, 3 and 2, and the CDB–P and $CaCO_3$ profiles were similar (Fig. 5). Calcite is able to rapidly bind significant amounts

of dissolved HPO_4^{2-} (Millero et al., 2001) and our experimental results showed that after 10 days, $CaCO_3$-bound P is extracted as exchangeable P and CDB-extractable P in equal amounts. However, the P K-edge XANES spectrum of disperse P resembles P adsorbed onto Al oxide or clay rather than $CaCO_3$ (Fig. 10). We propose that the high concentration of P (10 mmol L^{-1}) used in $CaCO_3$–P synthesis by Giguet-Covex et al. (2013) may have favored formation at the calcite surface of Ca–P (apatite) with the characteristic post-edge shoulder feature observed in their $CaCO_3$–P spectrum (Fig. 10). Phosphorus concentrations are three orders of magnitude lower in the Black Sea pore waters (10–20 μmol L^{-1}) and thus Ca–P formation at the calcite surface is less likely; this would lead to a more featureless spectrum indicative of adsorbed $CaCO_3$–P rather than Ca–P. It is possible that clay-bound P also was present and contributed to the disperse P K-edge spectra; clay minerals and $CaCO_3$ both make up about half of the investigated sediment samples on a weight basis. Polyphosphates are rapidly remineralized to dissolved HPO_4^{2-} under anoxic and sulfidic conditions (Brock and Schulz-Vogt, 2011; Diaz et al., 2012) and are therefore unlikely to represent a significant sedimentary P pool in the deep Black Sea.

Although adsorbed P is the main source of CDB-extractable P in the sulfidic sediments, the micro-scale XRF and X-ray absorption results did provide evidence for Fe–P in the deep Black Sea. A P enrichment with a spectrum very similar to that of the Fe(II) phosphate ludlamite was observed in the surface sediment of station 2 (<1 cm sediment depth, Fig. 9). Considering the highly unfavorable conditions for Fe–P formation here (400 μmol L^{-1} HS$^-$, no detectable dissolved Fe^{2+}), this enrichment likely represents Fe(II)- or Fe(III)–P that formed above or within the redox-cline and escaped sulfidization before settling onto the
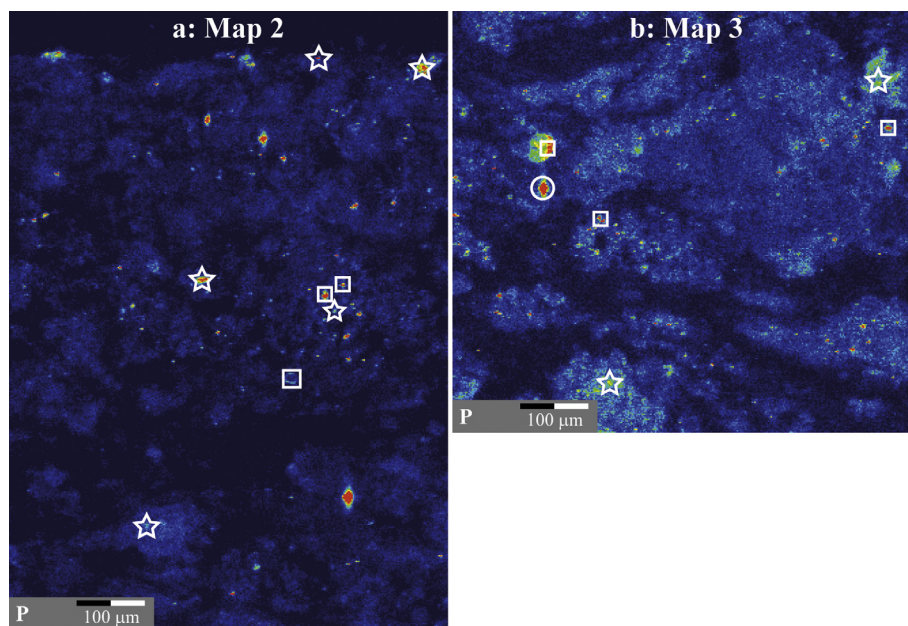

Fig. 9. Synchrotron-based μXRF mapping (4 μm^2 resolution) of phosphorus for Map 2 (a) and 3 (b) (see Fig. 6). Scale bar in bottom left corner. Symbols indicate spot XAS measurements of different types of P-bearing phases: apatite (square), ludlamite (circle) and adsorbed/organic PO$_4$ (star).

sediment surface. This suggests that Fe–P shuttling, which acts as a source of sediment P in deep (200 mbss) sulfidic Baltic Sea sediments (Jilbert and Slomp, 2013), can also deliver P to sediment at much greater water depths (2000 mbss). However, the spectroscopic data indicate that this P pool is of minor importance in the deep Black Sea: the Fe(II)–P enrichment accounted for around 5% of the total P fluorescence collected from mapped area 3 (Fig. 9). In mapped area 2, Fe(II)–P was likely equally or more scarce: all P enrichments that could be analyzed by spot P K-edge XANES consisted of apatite, and the summed fluorescence from all discrete

enrichments accounted for ~10% of total fluorescence. This is very similar to the relative abundance of authigenic and detrital Ca–P as determined by chemical extraction for station 2 surface sediment (10–15% of total P).

4.2. Benthic phosphorus dynamics and burial across the Black Sea redox gradient

Sedimentary P burial in the Black Sea shows marked changes along the depth transect. High sedimentary phosphorus contents were found in surface sediments on the
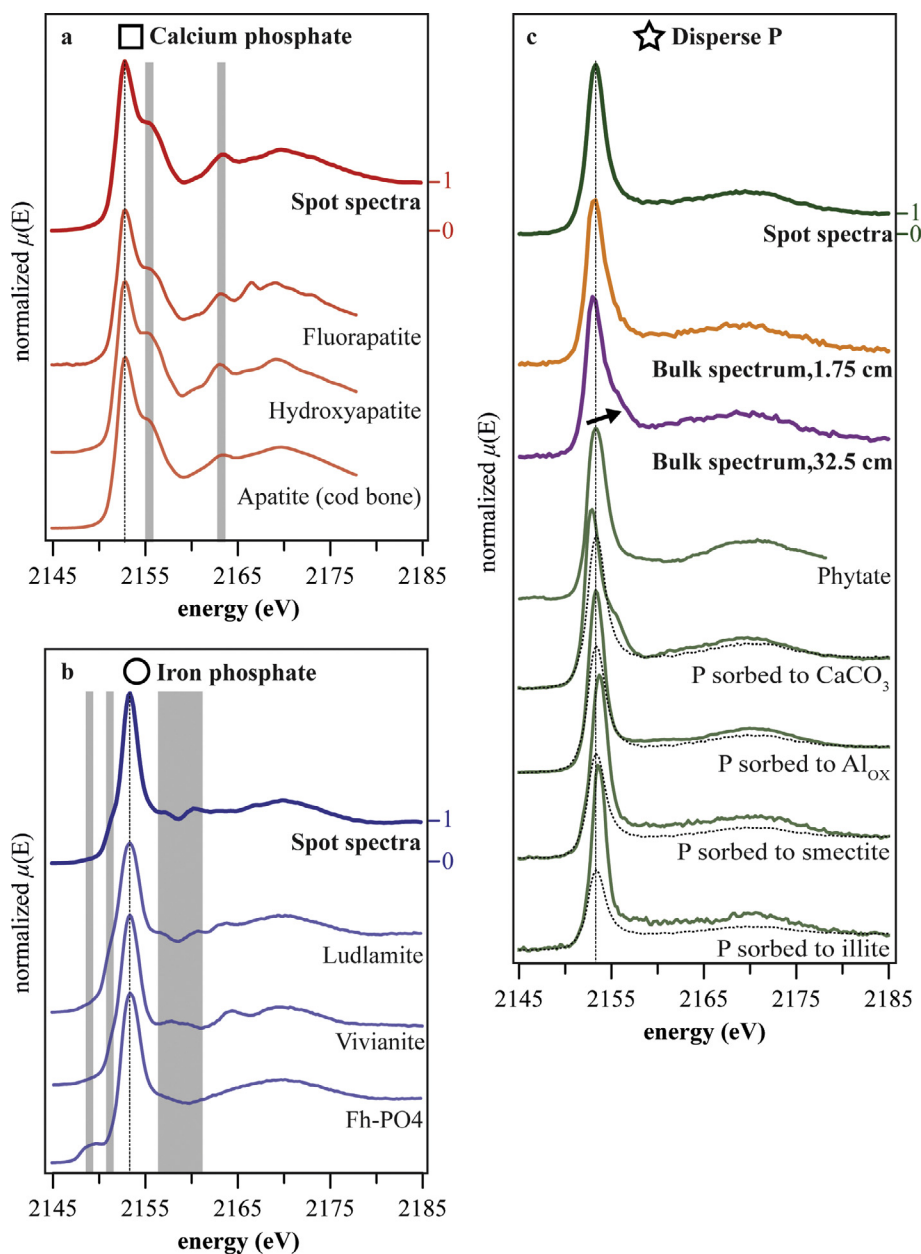

Fig. 10. Normalized P K-edge XANES spectra for selected spot measurements from Map 2 and 3 (see Fig. 9), as well as spectra of reference for calcium phosphate (a), iron-associated phosphate (b) and disperse P (c). In addition, P spectra collected from a surface and deep bulk sample from station 2 are included in (c). For comparison of white line position and peak height, the spectrum of disperse P from the sample is added as a dashed line. Here, the arrow indicates the development of a post-edge shoulder feature in the spectrum of the deep sample as found in Ca phosphates. Dashed lines are drawn to compare white line positions, gray bars indicate key absorption features for the various P phases.

shelf and in the redoxcline (stations 7, 6A and 6B) (Fig. 2). The low $C_{org}/P_{reactive}$ ratios reflect efficient P retention. Peak P contents were not found under well-oxygenated waters on the oxic shelf (150 μmol O_2 kg^{-1}), but under poorly oxygenated waters (~10 μmol O_2 kg^{-1}) in the redoxcline. Here, upward diffusing dissolved Fe^{2+} from the anoxic waters at the lower boundary of the redoxcline is exposed to oxygenated waters, leading to Fe^{2+} oxidation and the formation and deposition of Fe(III) (oxyhydr)oxides that adsorb PO_4 from the water column and pore water. This "P pump" (Shaffer, 1986) results in excess P retention in surface sediments around the redoxcline. As a result, Fe(III)-bound P is the most important P form in the surface sediment (50–60% of total P) at these stations, followed by organic P (~ 30% of total P). At depth in the sediment, highly reactive Fe(III) phases and Fe(III)-bound P decline and organic P becomes by far the most important P sink (~50% of total P). The absolute and relative increase in apatite P (acetate–P) with sediment depth at station 7 reflects authigenic Ca–P formation, i.e. transformation of more labile P reservoirs such as organic P to apatite. This process of 'sink switching' (Ruttenberg and Berner, 1993) was also observed in sediments from shallow water depths in the Black Sea by Dijkstra et al. (2014). Due to these redox-dependent processes, temporal fluctuations in the vertical extent of the redoxcline affect the formation or dissolution of Fe(III) (oxyhydr)oxides, and the surface sediment may switch between being a net sink or source for P.

Below the redoxcline at stations 4, 3 and 2, there is a slight decline in sedimentary P contents (Fig. 2) and a major change in the mechanisms by which P is buried in the sediment. A decrease in the sedimentary P retention efficiency under the sulfidic deep waters is reflected in a strong increase in the molar $C_{org}/P_{reactive}$ ratio from ~50 to ~250 (Fig. 3). Organic C is better preserved below the redoxcline, while P is liberated from the OM and recycled back to the overlying water in the absence of Fe(III) phases in the surface sediment (Ingall et al., 1993; Steenbergh et al., 2011). Furthermore, anoxic conditions can promote the release of P from organic matter (Gächter et al., 1988; Hupfer et al., 2004). In the sediment, detrital input of P declines with increasing water depth and distance to shore and Danube inflow, the main source of dissolved and particulate matter in the northwestern Black Sea. However, the sedimentary P/Al ratio increases with increasing water depth below the redoxcline (Fig. 12), likely because of the increased preservation of organic matter (the main P source) with water depth (Fig. 2). As such, both Fe and P become enriched relative to Al below the redoxcline (Fig. 12), but by different mechanisms. Phosphorus enrichment is directly linked to OM preservation. For Fe, there is a shelf-to-basin shuttle that is driven by reductive Fe dissolution from shelf sediment and formation of Fe(III) particles in the oxic shelf bottom waters. The Fe(III) particles are in part transported beyond the shelf break, eventually sink below the redoxcline where they are transformed to FeS_2 that settles and increases the Fe contents of the deep basin sediment (Wijsman et al., 2001; Lyons and Severmann, 2006).

There is a relative and absolute increase in the amount of CDB–P in the sediment with water depth for the deep stations. As discussed in Section 4.1, this CDB–P is likely not associated with Fe but rather represents P adsorbed onto sediment components such as $CaCO_3$ and clays. Our findings indicate that the dominant P sinks in the deep sulfidic sediments are ($CaCO_3$-) adsorbed and organic P, each making up ~30% of the total P reservoir.
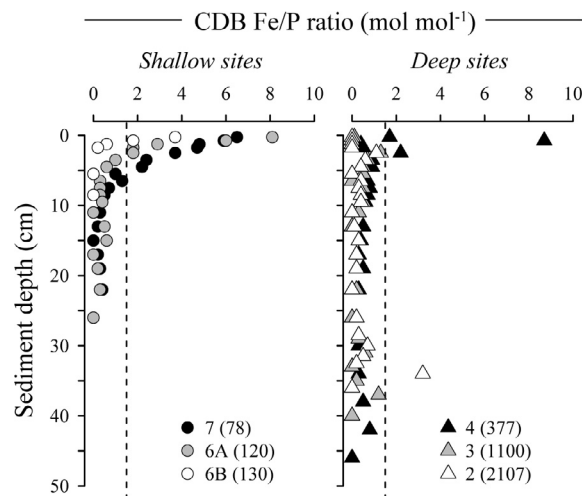

Fig. 11. Iron/phosphorus ratios in the CDB extracts from the shallow sites (left panel) and the deep sites (right panel). Vertical dashed line indicates the Fe/P ratio for Fe(II)–P minerals of 1.5. Legend shows station number with depth (mbss) between parentheses.
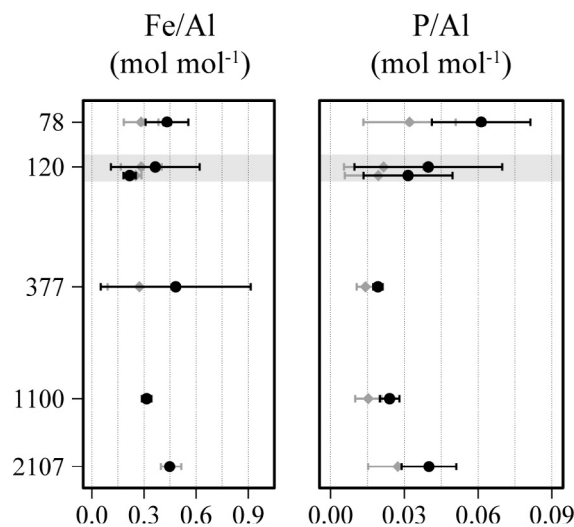

Fig. 12. Aluminum-normalized iron and phosphorus contents versus water depth. Black circles represent average of surface sediment (0–2 cm depth, $n = 4$), gray circles represent whole-core averages for each station ($n = 12$–24). Gray horizontal bars indicate the approximate position of the redoxcline. Error bars show standard deviation. Note the logarithmic y-axis, which is only labelled at station water depths (station number between parentheses).

The adsorbed P may be formed both in the water column and in the sediment. The increase in CDB–P at the Unit II/I transition contrasts with the trends in the other P reservoirs and indicates a change in P burial dynamics at the Unit II/I transition, with an increasingly important role for P adsorption onto/incorporation into the calcareous sediment matrix. There are no major changes in the

$C_{org}/P_{reactive}$ ratio from Unit II to Unit I, apart from a slight decrease at station 3, suggesting that changes in sedimentary P cycling did not strongly affect sedimentary P retention capacity. The absolute and relative increase in apatite P with sediment depth, in particular in the top part of the sediment, at the deep stations indicate that authigenic Ca–P formation also occurs in these highly
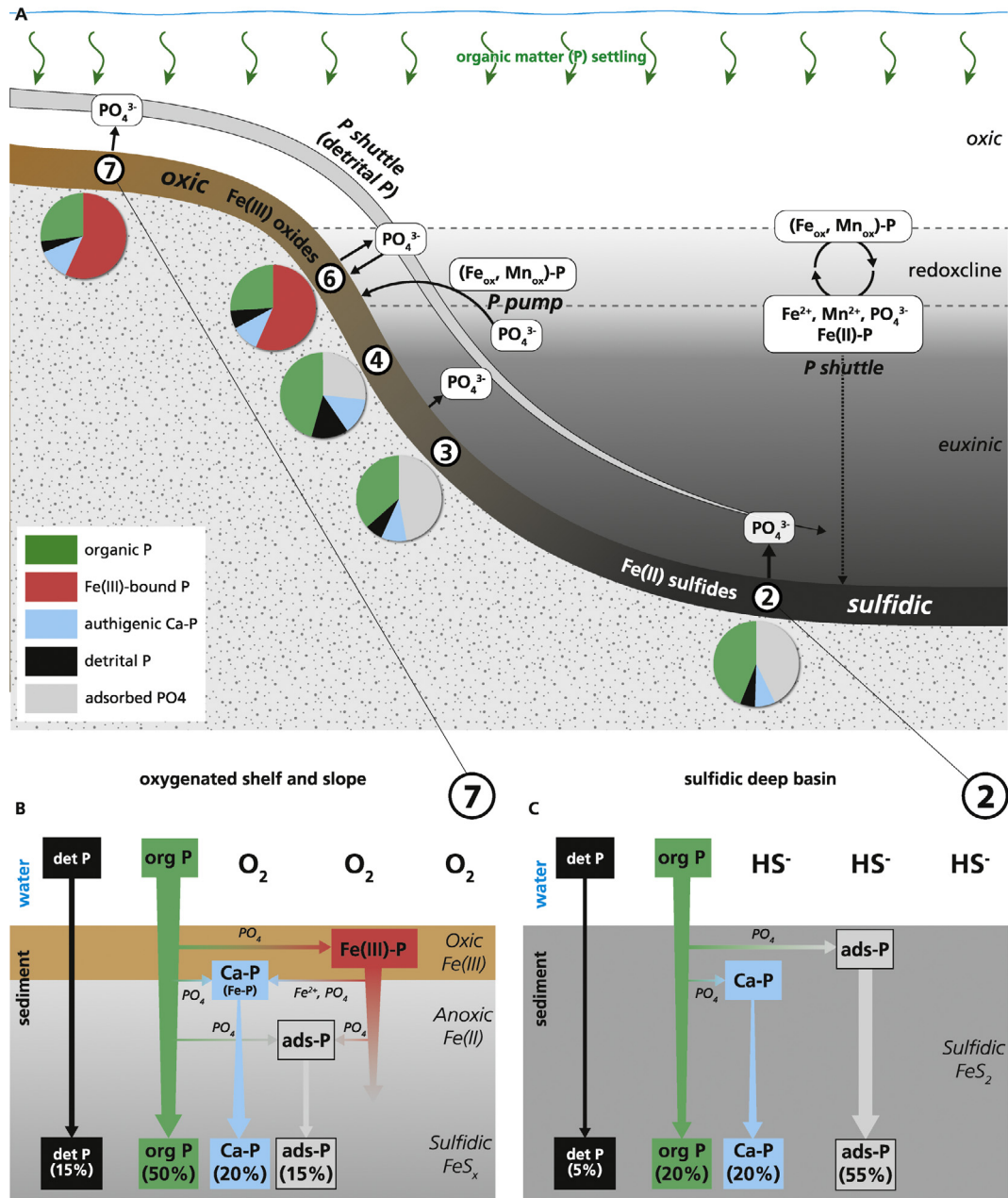

Fig. 13. Schematic overview of P cycling across the depth (redox) transect in the Black Sea. Panel A shows the overall trend in chemical P forms with water depth, with the relative P distribution in the surface sediment (0–2 cm, $n = 4$) shown as pie charts. We show both the P pump that enriches the surface sediment of the redoxcline in Fe(III)-bound P, and the P shuttle that may transfer Fe-associated P from the shelf or redoxcline into the deep basin. The P shuttle is depicted as a dashed line, as we did not find Fe-associated P to be quantitatively important in the deep basin and it may be derived from lateral transport from the shelf. Panel B and C show P diagenesis in surface sediments from the shelf with oxygenated bottom waters (station 7) and sulfidic deep basin (station 2), respectively. We assume that Fe-associated P under sulfidic conditions at depth in the shelf sediments and throughout the sediment of the sulfidic deep basin is negligible, and that any P extracted by CDB is in fact adsorbed P.

sulfidic sediments. In Unit I sediment at the deep stations, there is at least a twofold increase with depth in the absolute and relative contribution of apatite P, signifying the importance of stable authigenic Ca–P as a long-term P burial phase in the deep sulfidic Black Sea.

In summary, our results show a shift from Fe(III)-bound P to P adsorbed onto $CaCO_3$ and possibly clay surfaces from the shelf with oxygenated bottom waters to the sulfidic deep basin in the northwestern Black Sea, while organic P is a major P sink under all redox conditions (Fig. 13). With increasing sediment depth, Ca–P authigenesis leads to an increasingly important role for apatite as (long-term) P burial phase.

5. IMPLICATIONS

Calcium carbonate can play a key role in P retention in anoxic and sulfidic sediments, and may more generally be important for P retention in carbonate-rich sediments with low HPO_4^{2-} concentrations and thus limited P mineral authigenesis. This P pool is often overlooked; $CaCO_3$–P is generally considered a minor P pool that is extracted together with (and thus indistinguishable from) authigenic Ca–P (i.e. apatite) (Ruttenberg et al., 2003). In fact, our results show that $CaCO_3$–P is extracted in the step targeting Fe-associated P, which emphasizes the caution required when interpreting sequential chemical extraction results from (anoxic and sulfidic) sediments.

The results presented here show that this $CaCO_3$–P can persist for at least a few thousand years (Unit I represents ~2700 years), so there is potential for long-term P retention by $CaCO_3$. This mechanism may have contributed to P retention in carbonate-rich sediments during periods of wide-spread and prolonged anoxia and euxinia, for instance during Holocene sapropel formation in the Mediterranean Sea (Rohling et al., 2015) and during Cretaceous oceanic anoxic events in the proto-Atlantic and Tethys oceans (Jenkyns, 2010).

The relative role of $CaCO_3$-associated P also controls the sensitivity of P retention to pH changes; $CaCO_3$ is much more sensitive to proton-promoted dissolution than apatite (Amankonah et al., 1985; Ruben and Bennett, 1987) and Fe-associated P phases. Consequently, shifts in the calcite compensation depth over geological time could impact the P source/sink function of deep sea sediments. Specifically, a decline in pH in response to increased uptake of atmospheric carbon dioxide by the ocean, as observed in the past (e.g. the massive deep sea calcite dissolution during the Paleocene–Eocene thermal maximum; Zachos et al., 2005) and projected for the future, could alter benthic P release and affect marine primary productivity.

APPENDIX A. SUPPLEMENTARY DATA

Supplementary data associated with this article can be found, in the online version, at http://dx.doi.org/10.1016/j.gca.2017.01.042.

REFERENCES

Algeo T. J. and Ingall E. (2007) Sedimentary Corg: P ratios, paleocean ventilation, and Phanerozoic atmospheric pO2. *Palaeogeogr. Palaeoclimatol. Palaeoecol.* **256**, 130–155.

Amankonah J. O., Somasundaran P. and Ananthapadmabhan K. P. (1985) Effects of dissolved mineral species on the dissolution/precipitation characteristics of calcite and apatite. *Colloids Surf.* **15**, 295–307.

Anderson L. D., Delaney M. L. and Faul K. L. (2001) Carbon to phosphorus ratios in sediments: implications for nutrient cycling. *Global Biogeochem. Cyc.* **15**, 65–79.

APHA (2005) *Standard methods for the examination of water and wastewater*, 21st ed. American Public Health Association – American Water Works Association – Water Environment Federation.

Arthur M. A. and Dean W. E. (1998) Organic-matter production and preservation and evolution of anoxia in the Holocene Black Sea. *Paleoceanography* **13**, 395–411.

Bartlett J. K. and Skoog D. A. (1954) Colorimetric determination of elemental sulfur in hydrocarbons. *Anal. Chem.* **26**, 1008–1011.

Berner R. A. (1970) Sedimentary pyrite formation. *Am. J. Sci.* **268**, 1–23.

Brandes J. A., Ingall E. and Paterson D. (2007) Characterization of minerals and organic phosphorus species in marine sediments using soft X-ray fluorescence spectromicroscopy. *Mar. Chem.* **103**, 250–265.

Brock J. and Schulz-Vogt H. N. (2011) Sulfide induces phosphate release from polyphosphate in cultures of a marine Beggiatoa strain. *ISME J.* **5**, 497–506.

Burton E. D., Bush R. T., Johnston S. G., Sullivan L. A. and Keene A. F. (2011) Sulfur biogeochemical cycling and novel Fe–S mineralization pathways in a tidally re-flooded wetland. *Geochim. Cosmochim. Acta* **75**, 3434–3451.

Canfield D. E., Raiswell R. and Bottrell S. H. (1992) The reactivity of sedimentary iron minerals toward sulfide. *Am. J. Sci.* **292**, 659–683.

Claff S. R., Sullivan L. A., Burton E. D. and Bush R. T. (2010) A sequential extraction procedure for acid sulfate soils: partitioning of iron. *Geoderma* **155**, 224–230.

Degens E. T. and Ross D. A. (1974) The Black Sea—geology, chemistry, and biology. *AAPG Memoir* **20**.

Dellwig O., Leipe T., März C., Glockzin M., Pollehne F., Schnetger B., Yakushev E. V., Böttcher M. E. and Brumsack H.-J. (2010) A new particulate Mn–Fe–P-shuttle at the redoxcline of anoxic basins. *Geochim. Cosmochim. Acta* **74**, 7100–7115.

Diaz R. J. and Rosenberg R. (2008) Spreading dead zones and consequences for marine ecosystems. *Science* **321**, 926–929.

Diaz J. M., Ingall E. D., Snow S. D., Benitez-Nelson C. R., Taillefert M. and Brandes J. A. (2012) Potential role of inorganic polyphosphate in the cycling of phosphorus within the hypoxic water column of Effingham Inlet, British Columbia. *Global Biogeochem. Cyc* **26**.

Dijkstra N., Kraal P., Kuypers M. M. M., Schnetger B. and Slomp C. P. (2014) Are iron-phosphate minerals a sink for phosphorus in anoxic Black Sea sediments? *PLoS ONE* **9**, e101139.

Dijkstra N., Slomp C. P. and Behrends T. (2016) Vivianite is a key sink for phosphorus in sediments of the Landsort Deep, an intermittently anoxic deep basin in the Baltic Sea. *Chem. Geol.* **438**, 58–72.

Eckert S., Brumsack H.-J., Severmann S., Schnetger B., März C. and Fröllje H. (2013) Establishment of euxinic conditions in the Holocene Black Sea. *Geology* **41**, 431–434.

Egger M., Jilbert T., Behrends T., Rivard C. and Slomp C. P. (2015) Vivianite is a major sink for phosphorus in methanogenic coastal surface sediments. *Geochim. Cosmochim. Acta* **169**, 217–235.

Einsele W. (1936) Über die Beziehung des Eisenkreislaufs zum Phosphorkreislauf im eutrophen See. *Arch. Hydrobiol.* **29**, 664–686.

Froelich P. N., Arthur M. A., Burnett W. C., Deakin M., Hensley V., Jahnke R., Kaul L., Kim K. H., Roe K., Soutar A. and Vathakanon C. (1988) Early diagenesis of organic-matter in Peru continental-margin sediments – phosphorite precipitation. *Mar. Geol.* **80**, 309–343.

Gächter R., Meyer J. S. and Mares A. (1988) Contribution of bacteria to release and fixation of phosphorus in lake-sediments. *Limnol. Oceanogr.* **33**, 1542–1558.

Giguet-Covex C., Poulenard J., Chalmin E., Arnaud F., Rivard C., Jenny J. P. and Dorioz J. M. (2013) XANES spectroscopy as a tool to trace phosphorus transformation during soil genesis and mountain ecosystem development from lake sediments. *Geochim. Cosmochim. Acta* **118**, 129–147.

Hay B. J., Arthur M. A., Dean W. E., Neff E. D. and Honjo S. (1991) Sediment deposition in the Late Holocene abyssal Black Sea with climatic and chronological implications. 38. *Deep Sea Res.* **38**(Suppl. 2), S1211–S1235.

Hesterberg D., Zhou W., Hutchison K. J., Beauchemin S. and Sayers D. E. (1999) XAFS study of adsorbed and mineral forms of phosphate. *J. Synchrotron Radiat.* **6**, 636–638.

Hsu T.-W., Jiang W.-T. and Wang Y. (2014) Authigenesis of vivianite as influenced by methane-induced sulfidization in cold-seep sediments off southwestern Taiwan. *J. Asian Earth Sci.* **89**, 88–97.

Hupfer M., Rube B. and Schmieder P. (2004) Origin and diagenesis of polyphosphate in lake sediments: a ^{31}P NMR study. *Limnol. Oceanogr.* **49**, 1–10.

Ingall E. and Jahnke R. (1994) Evidence for enhanced phosphorus regeneration from marine sediments overlain by oxygen depleted waters. *Geochim. Cosmochim. Acta* **58**, 2571–2575.

Ingall E. D., Brandes J. A., Diaz J. M., de Jonge M. D., Paterson D., McNulty I., Elliott W. C. and Northrup P. (2011) Phosphorus K-edge XANES spectroscopy of mineral standards. *J. Synchrotron Radiat.* **18**, 189–197.

Ingall E. D., Bustin R. M. and Van Cappellen P. (1993) Influence of water column anoxia on the burial and preservation of carbon and phosphorus in marine shales. *Geochim. Cosmochim. Acta* **57**, 303–316.

Jenkyns H. C. (2010) Geochemistry of oceanic anoxic events. *Geochem. Geophys. Geosyst.* **11**, Q03004.

Jensen H. and Thamdrup B. (1993) Iron-bound phosphorus in marine sediments as measured by bicarbonate–dithionite extraction. *Hydrobiologia* **253**, 47–59.

Jilbert T. and Slomp C. P. (2013) Iron and manganese shuttles control the formation of authigenic phosphorus minerals in the euxinic basins of the Baltic Sea. *Geochim. Cosmochim. Acta* **107**, 155–169.

Kraal P., Bostick B. C., Behrends T., Reichart G.-J. and Slomp C. P. (2015a) Characterization of phosphorus species in sediments from the Arabian Sea oxygen minimum zone: Combining sequential extractions and X-ray spectroscopy. *Mar. Chem.* **168**, 1–8.

Kraal P., Burton E. D. and Bush R. T. (2013) Iron monosulfide accumulation and pyrite formation in eutrophic estuarine sediments. *Geochim. Cosmochim. Acta* **122**, 75–88.

Kraal P., Burton E. D., Rose A. L., Kocar B. D., Lockhart R. S., Grice K., Bush R. T., Tan E. and Webb S. M. (2015b) Sedimentary iron–phosphorus cycling under contrasting redox conditions in a eutrophic estuary. *Chem. Geol.* **392**, 19–31.

Kraal P. and Slomp C. P. (2014) Rapid and extensive alteration of phosphorus speciation during oxic storage of wet sediment samples. *PLoS ONE* **9**, e96859.

Kraal P., Slomp C. P. and de Lange G. J. (2010) Sedimentary organic carbon to phosphorus ratios as a redox proxy in Quaternary records from the Mediterranean. *Chem. Geol.* **277**, 167–177.

Kraal P., Slomp C. P., Forster A., Kuypers M. M. M. and Sluijs A. (2009) Pyrite oxidation during sample storage determines phosphorus fractionation in carbonate-poor anoxic sediments. *Geochim. Cosmochim. Acta* **73**, 3277–3290.

Kraal P., Slomp C. P., Reed D. C., Reichart G. J. and Poulton S. W. (2012) Sedimentary phosphorus and iron cycling in and below the oxygen minimum zone of the northern Arabian Sea. *Biogeosciences* **9**, 2603–2624.

Krom M. D. and Berner R. A. (1980) Adsorption of phosphate in anoxic marine sediments. *Limnol. Oceanogr.* **25**, 797–806.

Lomnitz U., Sommer S., Dale A. W., Löscher C. R., Noffke A., Wallmann K. and Hensen C. (2015) Benthic phosphorus cycling in the Peruvian oxygen minimum zone. *Biogeosci. Discuss.* **12**, 16755–16801.

Lyons T. W. and Severmann S. (2006) A critical look at iron paleoredox proxies: New insights from modern euxinic marine basins. *Geochim. Cosmochim. Acta* **70**, 5698–5722.

März C., Hoffmann J., Bleil U., de Lange G. J. and Kasten S. (2008a) Diagenetic changes of magnetic and geochemical signals by anaerobic methane oxidation in sediments of the Zambezi deep-sea fan (SW Indian Ocean). *Mar. Geol.* **255**, 118–130.

März C., Poulton S. W., Beckmann B., Küster K., Wagner T. and Kasten S. (2008b) Redox sensitivity of P cycling during marine black shale formation: Dynamics of sulfidic and anoxic, non-sulfidic bottom waters. *Geochim. Cosmochim. Acta* **72**, 3703–3717.

Middelburg J. J. and Levin L. A. (2009) Coastal hypoxia and sediment biogeochemistry. *Biogeosciences* **6**, 1273–1293.

Millero F., Huang F., Zhu X., Liu X. and Zhang J.-Z. (2001) Adsorption and Desorption of Phosphate on Calcite and Aragonite in Seawater. *Aquat. Geochem.* **7**, 33–56.

Mort H. P., Slomp C. P., Gustafsson B. G. and Andersen T. J. (2010) Phosphorus recycling and burial in Baltic Sea sediments with contrasting redox conditions. *Geochim. Cosmochim. Acta* **74**, 1350–1362.

Mortimer C. H. (1941) The exchange of dissolved substances between mud and water. *J. Ecol.* **29**, 280–329.

Murphy J. and Riley J. (1958) A single solution method for the determination of soluble phosphate in sea water. *J. Mar. Biol. Assoc. UK* **37**, 9–14.

Nembrini G. P., Capobianco J. A., Viel M. and Williams A. F. (1983) A Mössbauer and chemical study of the formation of vivianite in sediments of Lago Maggiore (Italy). *Geochim. Cosmochim. Acta* **47**, 1459–1464.

Petersen G. W., Chesters G. and Lee G. B. (1966) Quantitative determination of calcite and dolomite in soils. *J. Soil Sci.* **17**, 328–338.

Poulton S. W. and Canfield D. E. (2005) Development of a sequential extraction procedure for iron: implications for iron partitioning in continentally derived particulates. *Chem. Geol.* **214**, 209–221.

Raiswell R., Buckley F., Berner R. A. and Anderson T. F. (1988) Degree of pyritization of iron as a paleoenvironmental indicator of bottom-water oxygenation. *J. Sediment. Res.* **58**, 812–819.

Raiswell R. and Canfield D. E. (1998) Sources of iron for pyrite formation in marine sediments. *Am. J. Sci.* **298**, 219–245.

Reed D. C., Gustafsson B. G. and Slomp C. P. (2015) Shelf-to-basin iron shuttling enhances vivianite formation in deep Baltic Sea sediments. *Earth Planet. Sci. Lett.* **434**, 241–251.

Reed D. C., Slomp C. P. and de Lange G. J. (2011) A quantitative reconstruction of organic matter and nutrient diagenesis in Mediterranean Sea sediments over the Holocene. *Geochim. Cosmochim. Acta* **75**, 5540–5558.

Reichart G. J., Den Dulk M., Visser H. J., Van der Weijden C. H. and Zachariasse W. J. (1997) A 225 kyr record of dust supply, paleoproductivity and the oxygen minimum zone from the Murray ridge (northern Arabian sea). *Palaeogeogr. Palaeoclimatol. Palaeoecol.* **134**, 149–169.

Rickard D. and Morse J. W. (2005) Acid volatile sulfide (AVS). *Mar. Chem.* **97**, 141–197.

Rivard C., Lanson B. and Cotte M. (2015) Phosphorus speciation and micro-scale spatial distribution in North-American temperate agricultural soils from micro X-ray fluorescence and X-ray absorption near-edge spectroscopy. *Plant Soil*, 1–16.

Rohling E. J., Marino G. and Grant K. M. (2015) Mediterranean climate and oceanography, and the periodic development of anoxic events (sapropels). *Earth-Sci. Rev.* **143**, 62–97.

Ruben J. A. and Bennett A. A. (1987) The evolution of bone. *Evolution* **41**, 1187–1197.

Ruttenberg K. C. (1990) *Diagenesis and burial of phosphorus in marine sediments: implications for the marine phosphorus budget*. Yale University, New Haven, p. 375.

Ruttenberg K. C. (1992) Development of a sequential extraction method for different forms of phosphorus in marine sediments. *Limnol. Oceanogr.* **37**, 1460–1482.

Ruttenberg K. C. and Berner R. A. (1993) Authigenic apatite formation and burial in sediments from non-upwelling, continental-margin environments. *Geochim. Cosmochim. Acta* **57**, 991–1007.

Ruttenberg K. C., Holland H. D. and Turekian K. K. (2003) The global phosphorus cycle. In *Treatise on Geochemistry* (ed. W. H. Schlesinger). Pergamon, Oxford, pp. 585–643.

Salomé M., Cotte M., Baker R., Barrett R., Benseny-Cases N., Berruyer G., Bugnazet D., Castillo-Michel H., Cornu C., Fayard B., Gagliardini E., Hino R., Morse J., Papillon E., Pouyet E., Rivard C., Solé V. A., Susini J. and Veronesi G. (2013) The ID21 scanning X-ray microscope at ESRF. *J. Phys. Conf. Ser.* **425**, 182004.

Schenau S. J. and De Lange G. J. (2000) A novel chemical method to quantify fish debris in marine sediments. *Limnol. Oceanogr.* **45**, 963–971.

Schenau S. J., Slomp C. P. and De Lange G. J. (2000) Phosphogenesis and active phosphorite formation in sediments from the Arabian Sea oxygen minimum zone. *Mar. Geol.* **169**, 1–20.

Schlitzer, R., 2015. Ocean Data View.

Schulz H. N. and Schulz H. D. (2005) Large sulfur bacteria and the formation of phosphorite. *Science* **307**, 416–418.

Shaffer G. (1986) Phosphate pumps and shuttles in the Black Sea. *Nature* **321**, 515–517.

Slomp C. P., Epping E. H. G., Helder W. and Van Raaphorst W. (1996a) A key role for iron-bound phosphorus in authigenic apatite formation in North Atlantic continental platform sediments. *J. Mar. Res.* **54**, 1179–1205.

Slomp C. P., Mort H. P., Jilbert T., Reed D. C., Gustafsson B. G. and Wolthers M. (2013) Coupled dynamics of iron and phosphorus in sediments of an oligotrophic coastal basin and the impact of anaerobic oxidation of methane. *PLoS One* **8**, e62386.

Slomp C. P., Van der Gaast S. J. and Van Raaphorst W. (1996b) Phosphorus binding by poorly crystalline iron oxides in North Sea sediments. *Mar. Chem.* **52**, 55–73.

Steenbergh A. K., Bodelier P. L. E., Hoogveld H. L., Slomp C. P. and Laanbroek H. J. (2011) Phosphatases relieve carbon limitation of microbial activity in Baltic Sea sediments along a redox-gradient. *Limnol. Oceanogr.* **56**, 2018–2026.

Suess E. (1979) Mineral phases formed in anoxic sediments by microbial decomposition of organic matter. *Geochim. Cosmochim. Acta* **43**, 339–352.

Tsandev I., Reed D. C. and Slomp C. P. (2012) Phosphorus diagenesis in deep-sea sediments: Sensitivity to water column conditions and global scale implications. *Chem. Geol.* **330–331**, 127–139.

Turekian K. K. and Wedepohl K. H. (1961) Distribution of the elements in some major units of the Earth's crust. *Geol. Soc. Am. Bull.* **72**, 175–192.

Van Cappellen P. and Berner R. A. (1988) A mathematical model for the early diagenesis of phosphorus and fluorine in marine sediments; apatite precipitation. *Am. J. Sci.* **288**, 289–333.

Wijsman J. W. M., Middelburg J. J. and Heip C. H. R. (2001) Reactive iron in Black Sea Sediments: implications for iron cycling. *Mar. Geol.* **172**, 167–180.

Wilkin R. T., Arthur M. A. and Dean W. E. (1997) History of water-column anoxia in the Black Sea indicated by pyrite framboid size distributions. *Earth Planet. Sci. Lett.* **148**, 517–525.

Zachos J. C., Röhl U., Schellenberg S. A., Sluijs A., Hodell D. A., Kelly D. C., Thomas E., Nicolo M., Raffi I., Lourens L. J., McCarren H. and Kroon D. (2005) Rapid acidification of the ocean during the paleocene-eocene thermal maximum. *Science* **308**, 1611–1615.

Associate editor: Thomas Wagner